

## Marine Sun Photometry Using Complementary Techniques

Mark A. Miller<sup>\*(1)</sup>, Kirk Knobelspiesse<sup>(3)</sup>, Robert Frouin<sup>(2)</sup>, Mary Jane Bartholomew<sup>(1)</sup>,  
R. Michael Reynolds<sup>(1)</sup>, Christophe Pietras<sup>(5)</sup>, Giulietta Fargion<sup>(5)</sup>, P. Quinn<sup>(6)</sup>  
and François Thieuleux<sup>(7)</sup>

Submitted to the Journal of Atmospheric and Oceanic Technology  
February 2004

<sup>\*(1)</sup> Earth System Science Division, Bldg. 490D, Brookhaven National Laboratory, Upton, NY 11973 (Corresponding Author)

<sup>(2)</sup> Scripps Institution of Oceanography, University of California San Diego, La Jolla, CA

<sup>(3)</sup> Science Systems and Applications, Inc., NASA SIMBIOS Project, Goddard Space Flight Center, Greenbelt, Maryland, USA

<sup>(4)</sup> University of Maryland Baltimore County, NASA SIMBIOS Project, Goddard Space Flight Center, Greenbelt, Maryland, USA

<sup>(5)</sup> Science Applications International Corp., NASA SIMBIOS Project, Goddard Space Flight Center, Greenbelt, Maryland, USA

<sup>(6)</sup> Pacific Marine Environmental Laboratory, Seattle Washington, USA

<sup>(7)</sup> Laboratoire d'Optique Atmosphérique, Université des Sciences et Technologies de Lille, Villeneuve d'Ascq, France

\* Corresponding Author email address: [miller@bnl.gov](mailto:miller@bnl.gov)

Running Title: Marine Sun Photometry during ACE-Asia

## ABSTRACT

Measurements collected aboard the R/V Ronald H. Brown during ACE-Asia are used to evaluate the capability of using complementary instrumentation to obtain the best possible estimates of aerosol optical thickness and Angstrom Exponent. Marine sun photometers deployed aboard the ship included two Microtops hand-held sun photometers, two research-grade hand-held sun photometers, and a Fast-Rotating Shadowband Radiometer. A wide range of aerosol conditions was encountered during the ACE-Asia cruise, including clean maritime conditions and highly polluted coastal environments. The results of this study suggest that the use of either hand-held or FRSR marine sun photometers to measure the aerosol optical thickness ( $\tau_{1A}$ ) in 10-nm wide bands in the visible and near-infrared regions yields similar results if proper measurement protocols are used and if the instruments are properly calibrated, so the data can be used interchangeably. The automated FRSR has significantly better temporal resolution (2-minutes) than the hand-held sun photometers when standard protocols and captures the local aerosol structure in polluted regions. Conversely, results suggest that the hand-held sun photometers may perform better in clean, maritime air masses, possibly because the environment is more cloudy, which challenges the automated cloud filtering algorithm used with the FRSR. Results also show that the statistical distribution of the Angstrom Exponent ( $\alpha$ ) during this experiment is different for the combined data from the hand-held sun photometers and the FRSR, and that these differences may arise from a combination of factors.

## 1.0 Introduction

The radiation transfer properties of tropospheric aerosols are one of the largest sources of uncertainty in climate models (NRC, 1996). The uncertainty is particularly acute over the world's oceans because there is a lack of *in situ* measurements that can be used to quantify the spatial distribution, chemical composition, and radiation-transfer characteristics of the aerosols in the marine atmosphere. Satellites play an essential role in characterizing the global distribution of over-ocean aerosols while *in situ* measurements are used to study local aerosol processes and to validate the satellite data in specific locations. The need for accurate *in situ* surveys of marine aerosol properties during the past decade has stimulated rapid progress in over-ocean sun photometry, which is the subject of this paper.

Sun photometers measure two fundamental quantities that describe the attenuating characteristics of the turbid atmosphere: the aerosol optical thickness,  $t_{\lambda}$ , and Ångström Exponent,  $a$  (Angstrom, 1961). The former is a coefficient describing the reduction in the direct-normal irradiance due to aerosols in a narrow channel centered on wavelength,  $\lambda$ , and the latter quantifies the wavelength dependence of  $t_{\lambda}$ . Sun photometers are difficult to operate at sea because they are sensitive to platform motion. Nonetheless, substantial progress has been made and new instruments and techniques have emerged. These include simple, commercially available hand-held devices (Microtops; Porter et al., 2001, Morys et al., 2001), more sophisticated, research-grade hand-held devices (Simbad and SimbadA; Deschamps et al., 2003), and marine Fast-Rotating Shadow-band Radiometers (FRSRs; Reynolds et al., 2001, Miller et al., 2004). All of these sun photometers are passive and measure the narrow-band optical thickness,  $t_{\lambda}$ , where  $\lambda$  is wavelength, in 10-nm wide channels scattered across the visible and near-infrared spectrum. Additionally, the FRSRs decompose the irradiance field into direct-normal and diffuse components, which can be used to retrieve additional information about the nature of the aerosol.

The purpose of this paper is to compare and evaluate the sun photometers that are being used to measure  $t_{\lambda}$  and  $a$  from ships at sea, and to provide guidance for the handling, processing, and interpretation of these data. Sun photometers and other instruments deployed aboard the R/V Ronald H. Brown during the Aerosol Characterization Experiment-Asia (ACE-Asia), which was conducted in the vicinity of eastern Asia, are analyzed and a technique to provide a "best-estimate" sun photometer time series of  $t_{\lambda}$  and  $a$  proposed. Previous measurements of the aerosol optical thickness time series from the R/V Ronald H. Brown during ACE-Asia have been published (Markowitz et al., 2003), but they were collected using a single commercial hand-held sun photometer. The measurements presented here are a consensus of the aerosol optical thickness measurements collected using three different techniques in conjunction with a dutiful uncertainty analysis. The ACE-Asia data demonstrate a wide range of issues related to the use of over-ocean radiation and aerosol measurements, and provides an excellent medium for instrument and technique evaluation.

## 2.0 The Data Set

The R/V Ronald H. Brown left Hawaii on 15 March 2001 and traveled across the North Pacific Ocean at latitude approximately 30-35 N (Figure 1a). The ship subsequently passed into the Philippine Sea, around the southern tip of Japan, through the northern part of the East China Sea, and into the Sea of Japan where it followed a complex trajectory (Figure 1b). During periods when cloud conditions permitted, measurements of  $t_1$  and  $a$  were collected with two Microtops sun photometers, one Simbad and one advanced Simbad (SimbadA) radiometer, and an FRSR. A Total Sky Imager (TSI) was used to obtain a visual assessment of the sky condition at the time of the measurement. Based on back trajectories (Draxler, 1992), seven relatively distinct aerosol regimes were encountered: marine, polluted, heavily polluted, polluted and dusty, polluted and less dusty, moderately polluted, and polluted but rainy (Figure 1a-b). Aerosol characterization on the basis of back trajectories was not possible for a small portion of the cruise trajectory. As the plot shows, generally polluted and dusty conditions were encountered in the vicinity of Japan, particularly in the Sea of Japan.

### 2.1. Sun Photometers

Each sun photometer used on the R/V Ronald H. Brown during ACE-Asia arrives at an estimate of the direct-normal irradiance using a slightly different method, but all use the Langley technique to determine the extra-terrestrial irradiance that is used to compute  $t_1$ . The Simbad, SimbadA, and Microtops are collimated radiometers with several narrow pass-bands that are manually pointed toward the sun to measure the direct-normal component of solar irradiance. The FRSR determines the direct-normal irradiance by subtracting an estimate of the diffuse irradiance made by occulting the solar disk with a mechanical arm from a measurement of the total hemispheric irradiance (Reynolds et al., 2001; Miller et al., 2004). An adjustment is made to account for the portion of the diffuse component inadvertently occulted by the arm during the diffuse measurement. A summary of the instruments used in this study is given in Table 1.

The application of sun photometry on a ship has the special problem of ship motion. The ship has a periodic rocking motion with a typical period of 5-15 s, and a mean tilt, which can be related to weight distribution, wind forcing, and the directional wave field. It will change slowly over hours or days, and more suddenly if the ship makes an abrupt direction change. Rocking is typically  $\pm 1-5^\circ$  on the R/V Ronald H. Brown, while the mean tilt can be  $\pm 1-2^\circ$ . Each radiometric technique used to measure  $t_1$  and  $a$  on the ship during ACE-Asia accommodates ship motion in a different manner. The operator mechanically stabilizes the hand-held devices, while the FRSR compensates for ship motion by measuring platform motion and compensating for it in post-processing.

#### 2.1.1 Hand-Held Instruments

Two Microtops hand-held sun photometers were used aboard the R/V Ronald H. Brown during ACE-Asia. They were manufactured by Solar Light Inc. and operated by representatives from the NASA Sensor Intercomparison and Merger for Biological

Oceanographic Studies (SIMBIOS Project) and the National Oceanic and Atmospheric Administration's Pacific Marine Environmental Laboratory (NOAA-PMEL), respectively. Complementing these instruments were two research-grade hand-held sun photometers (Simbad and SimbadA) designed by Laboratoire d'Optique Atmosphérique of the University of Lille, France. All of these hand-held sun photometers measure  $t_I$  in several spectral bands of approximately 10-nm width and measurements are taken when the observer deems the sky to be clear of clouds. Radiation captured by a collimator through a lens falls upon photodiode detectors, which produce an electrical current proportional to the radiant energy. There is a visual targeting mechanism to enable the user to manually aim the collimator in the direction of the solar disk. For Simbad, SimbadA, and Microtops, several measurements over a period of seconds are collected to form a measurement. Uncertainties for the Simbad and SimbadA hand-held units are estimated in the published literature to be 0.012-0.019 (Deschamps et al., 2004) and uncertainties for the Microtops units are thought to be similar.

An important issue, especially in marine conditions, is the sampling strategy. The normal measurement sensitivity to the dexterity of the user is compounded by ship motion, thereby influencing measurement accuracy through sun pointing errors (Porter et al., 2001). Sun pointing errors bias the measurements toward higher values of  $t_{IA}$ . Early deployments of Microtops on ships used the manufacturer-supplied measurement protocol to determine  $t_{IA}$ , but later studies showed that this default protocol could introduce significant uncertainty on a moving platform. The SIMBIOS Microtops uses a specially designed protocol and post-processing algorithm to remove this effect (Knobelspiesse et al., 2002). The SIMBIOS Microtops measurement protocol is to collect twenty samples over a six-second period and store the sample with the largest voltage, which is used to compute  $t_{IA}$ . After the experiment, a post-processing algorithm is used to further screen measurements to remove sun-pointing errors. The data are naturally grouped into discrete segments corresponding to a period of several minutes. For each sample period, a Coefficient of Variation (CoV) is computed by dividing the standard deviation of the measurement set by its mean. If the CoV is above a threshold of 0.05, the highest value of  $t_{IA}$  is removed and the CoV recomputed. This iteration continues until the CoV is less than the threshold or there are not enough points to compute the standard deviation. Data are only accepted if the iteration is successful in all measurement bands.

The SIMBIOS protocol was used for one Microtops during ACE-Asia, while the manufacturer-supplied protocol was supposed to be used for the PMEL Microtops. The manufacturer-supplied default protocol is to average the four lowest  $t_{IA}$  samples out of a set of thirty-two. Unfortunately, the PMEL Microtops was mistakenly set to average the lowest *twenty* measurements out of the thirty-two, which appreciably increased measurement uncertainty. A post-processing algorithm was employed to make the PMEL Microtops data consistent with the SIMBIOS protocol. Measurements whose standard deviation in the twenty averaged samples exceeded the published uncertainty of the SIMBIOS protocol were removed (0.015, Pietras et al., 2002). Therefore, relatively few measurements from the PMEL Microtops were available for analysis.

The Simbad and SimbadA protocol is conceptually similar to the Microtops manufacturer-supplied protocol, but with a higher sampling rate that makes them less

sensitive to platform motion. Each series of Simbad and SimbadA  $t_{IA}$ 's are collected during a ten-second period at ten-Hertz frequency, so one hundred samples are collected during the measurement period. The lowest sample  $t_{IA}$ 's are averaged to determine  $t_{IA}$  for the ten-second measurement period. The higher sampling frequency of the Simbad and SimbadA increases the probability that samples will be collected exclusively along the direct-normal solar vector.

The hand-held sun photometers were calibrated before and after the ACE-Asia experiment. Two calibration methods were used: the Langley technique or a calibration transfer procedure (Table 2). The Langley technique is to measure direct-normal irradiance in clear skies at various solar zenith angles and extrapolate in log-space to predict the magnitude of the signal at the top of the atmosphere. The Langley technique requires exceptionally clear conditions such as those encountered at sites such as the high altitude observatory at Mauna Loa, Hawaii. The calibration transfer method uses concurrent measurements from an uncalibrated sun photometer and adjusts them to be consistent with a calibrated instrument. Reference instruments used by the SIMBIOS project are sun photometers calibrated at Mauna Loa every three months.

### 2.1.2 The Marine Fast-Rotating Shadow-Band Radiometer

The marine FRSR used on the R/V Ronald H. Brown used a seven-channel (one broad-band, six 10-nm narrow-band) silicon-detector-based optical head and a semi-circular occulting arm (Reynolds et al., 2001). The FRSR was placed aboard the ship approximately two months prior to the beginning of the ACE-Asia campaign. The occulting arm circumscribes a complete rotation centered on the optical head, thereby occulting a band of the sky, with a revisitation period of 6.5 s. The signals from all seven optical channels are sampled rapidly, so the shadow cast by the shadow-band onto the detectors can be recognized and recorded. Ship motion is compensated mathematically through careful accounting of platform position.

The Langley technique was used to calibrate the FRSR before and after ACE-Asia because a calibration could not be used at sea due to platform orientation uncertainty (Miller et al., 2004). Langley calibrations of FRSRs on land generally provide values of the extra-terrestrial irradiance that agree within 1-2% of a specific published solar spectra (Thuillier et al., 2002). Extra-terrestrial irradiances used to process FRSR data for the ACE-Asia campaign are derived by convolving the instrument band-pass with a specific extra-terrestrial solar spectral irradiance, rather than through frequent Langley analyses, as would be the case on land. Because the FRSR is deployed for extended periods, the instrument gain is continuously monitored by comparing the broadband channel with more stable broadband measurements from a coincident Eppley pyranometer mounted on the FRSR platform. Instrument gains are adjusted in post-processing in an attempt to maintain a calibration consistent with the specified reference extra-terrestrial irradiance, though the data can always be adjusted to be consistent with other published extra-terrestrial irradiances (Miller et al., 2004).

The FRSR differs from hand-held sun photometers because it collects data continuously. Because the marine boundary layer is particularly cloudy environment, measurements of  $t_{IA}$  are often contaminated by  $t_{IC}$ , the optical thickness of clouds. In the case of hand-held sun photometers, the operator filters clouds by taking observations

at times when the sun's disk is completely visible. The FRSR collects data continuously, which dictates that cloud contamination will be naturally included in the data record since there is no initial subjective filtering. Therefore, an automatic cloud-filtering algorithm is required.

The conceptual foundation of the FRSR cloud filter is the differing levels of variability observed in the two signals,  $t_{IA} + t_{IC}$  and  $t_{IA}$ . Broken cloud fields show large variations in  $t_I$  as clouds drift across the solar disk. In contrast,  $t_{IA}$  is reasonably constant over periods of an hour or two due to the time scales of the physical processes that modulate changes in the aerosol load. Observations are considered individually in the cloud filter and scatter between neighboring observations is the key filtering metric. In addition to this automated filtering technique, a small percentage of the remaining data points are manually filtered because cloud contamination is obviously present. While this cloud filtering technique does contain a subjective element, comparison with other sun photometers shown later in this paper and in other studies attest to its validity.

The uncertainty in FRSR measurements has been rigorously analyzed using data and error propagation models (Miller et al., 2004). The uncertainty in  $t_{IA}$  is approximately 0.03 at low zenith angles and 0.02 at high zenith angles. This uncertainty can degrade to 0.04 at low solar zenith angles if the gain of the instrument drifts significantly over the duration of a deployment.

## 2.2 Total Sky Imager

It is often convenient to have a visual reference from which to evaluate sky condition. A Total Sky Imager (TSI) provides continuous digitization of the hemispheric sky condition and computes cloud amount for each image (Long et al., 2001). The TSI used on the R/V Ronald H. Brown during ACE-Asia was a modified version of the Model 880 manufactured by Yankee Environmental Systems Incorporated. For ship operation, a spherical dome control system that compensates for ship motion was designed at Brookhaven National Laboratory. The dome rotates in response to continuous information about ship heading so that a black Velcro strip always occludes the sun. The TSI software produces both images and a quantitative estimate of cloud fraction for each minute of the day, although only the visual images are used in this paper.

## 3.0 Sun Photometer Data Quality Evaluations and Comparisons

A key problem in the analysis of the aerosol optical data collected during ACE-Asia is arriving at a consensus for the value of  $t_{IA}$  when it is being measured using several instruments with different calibrations and spectral bandpasses. A fundamental issue is the calculation of  $a$ , often computed using only two spectral bands, when the measurements of  $t_{IA}$  from different instruments have varying spectral bandpasses. To circumvent this problem, a fit to all  $t_{IA}$ 's was used to compute  $a$ . As discussed below, however, this  $a$  fitting technique produces uncertainty artifacts that must be considered in this analysis. There is a fundamental disagreement in the value of  $t_{IA}$  measured by the Simbad and FRSR bands with band centers <440-nm, which has serious implications

for the calculation of  $\mathbf{a}$ . Because it is not possible to determine which of the two measurements is correct from this data set, these data are excluded from further analysis.

To form the necessary data set for a direct comparison of the measurements from the five instruments, a fifteen-minute window surrounding the individual measurement from one instrument is prescribed. A search through the data set is performed to identify measurements from the other instruments (similar bands, within 10-nm) that fall within this window. The temporally closest measurement within the fifteen-minute window is used as the comparison data point. Comparisons of  $t_{490-500A}$  and  $\mathbf{a}$  are shown as scatterplots (Figures 2, 3, 4, 5) and comparison results in other measurement bands are tabularized (Table 2). Comparison data that agree within uncertainties are indicated on the plots along with the percentage of points that meet these criteria. Although only  $t_{490-500A}$  scatterplots are shown, scatterplots for other  $t_{IA}$ 's show similar relationships when the instruments are compared (Table 2). The PMEL Microtops data have been omitted from the scatterplots because the number of comparison data points after pointing-uncertainties have been filtered is one to two orders of magnitude lower than the other comparisons (these data are included in the tabularized results).

The  $t_{490-500A}$  scatterplots for the hand-held units show good agreement in slope and relatively small scatter (Figure 2). Although the scatter is slightly larger, the agreement in  $\mathbf{a}$  for the hand held units is also quite good, especially considering the larger uncertainty implicit in measurements of  $\mathbf{a}$ , particularly at low  $t_{IA}$  (Figure 3). This source of uncertainty can be demonstrated by propagating the uncertainty in a simple two-wavelength calculation of  $\mathbf{a}$ . This uncertainty is expressed as

$$\mathbf{s}_a^2 = \underbrace{\left\{ \ln \left( \frac{I_1}{I_2} \right) \right\}^{-2}}_{\text{Band-Separation}} \underbrace{\left[ \left( \frac{\mathbf{s}_{t_{I1}}}{t_{I1}} \right)^2 + \left( \frac{\mathbf{s}_{t_{I2}}}{t_{I2}} \right)^2 \right]}_{\text{AOT}}, \quad (1)$$

where  $\mathbf{s}_a^2$  is the  $\mathbf{a}$  uncertainty (Miller et al., 2004). As indicated in (1),  $\mathbf{s}_a^2$  is proportional to the inverse square of  $t_{IA}$  (the AOT term), a characteristic that contributes to scatter in the  $\mathbf{a}$  comparisons. This is illustrated by plotting the ratio of  $\mathbf{a}$ 's from each instrument versus the average  $t_{490-500A}$  for the two instruments (Figure 4). The Microtops/Simbad plot, which is a particularly good example of this sun photometer uncertainty property, demonstrates increased scatter in the  $\mathbf{a}$  ratio when  $t_{490-500A}$  becomes small. Another caveat of the  $\mathbf{a}$  comparisons that is not demonstrated by the two-wavelength error propagation calculation shown in (1) is generated by the use of a line fit to the  $t_{IA}$  data to compute  $\mathbf{a}$ . The uncertainty in this method is sensitive to the number of channels and the distribution of channels across the visible and near-infrared spectrum that is used in the line fit. Ideally, comparisons between instruments should be made using line fits based on the same number of channels and approximately the same channel locations across spectrum. Moreover, the band-separation term in (1) shows that the separation between the two bands contributes to uncertainty. This sensitivity is exhibited when a line fit is used.

The FRSR to hand-held comparison scatterplots (Figure 5) show systematic FRSR underestimation of  $t_{490-500A}$  when  $t_{490-500A} > 0.5$ . This disagreement is traced to difficulties with the shadow-band technique due to enlargement in the solar aureole in highly polluted air masses, and is consistent across all bands (Miller et al., 2004). Images from the TSI illustrate the two extremes in sky condition encountered during the cruise: a clean, maritime air mass over the Northern Pacific Ocean (Figure 6a) and a highly polluted air mass over the Sea of Japan (Figure 6b). The figure shows extremely blue sky and modest whitening at the horizon in the clean air mass. In contrast, in the polluted air mass the horizon has a brownish color and that the entire sky appears to be dull and whitened. The reduction in total irradiance between the two air masses is graphically illustrated by comparing the brightness of the ship's superstructure in the two images. The solar aureole, which is the faintly colored luminous ring that surrounds the sun's disk through the haze, is significantly larger and brighter in the polluted air mass.

The enlarged solar aureole in highly polluted air masses (and when thin cirrus is present) necessitated an adjustment in the FRSR sweep-level processing (Miller et al., 2004). This is because the direct beam irradiance is computed using the difference between the shadow irradiance and the edge irradiance, which is the irradiance just before the occulting band reaches the edge of the solar disk (Reynolds et al., 2001). When an air mass is clean and the solar aureole is minimal, well-defined edge-shadow irradiances can be determined from the individual sweeps within the two-minute data collection window (Figure 6a). The variability from sweep-to-sweep is caused by ship motion and instrument response (Miller et al., 2004). In contrast, the solar aureole is much less defined in the polluted air mass (Figure 6b). This situation requires that a non-linear, curve-fitting scheme be employed to determine the edge irradiance. Most importantly, the state-of-the-sky as inferred from individual sweep data from the FRSR and visual evidence from the TSI clearly suggests that multiple scattering cannot be ignored in this highly polluted environment. Despite improvements in the  $t_{490-500A}$  shadow-band algorithm, this bias still exists, though it is considerably smaller than the bias associated with the algorithm used prior to this analysis. Hence, caution must be exercised when interpreting FRSR measurements if  $t_{490-500A} > 0.5$ .

The  $a$ 's inferred from the measurements of  $t_{490-500A}$  generally agree within uncertainties (>65% of the time when compared to Microtops and >73% when compared to Simbad and SimbadA), although the plots suggest that the FRSR has a tendency to overestimate  $a$  (Figure 7). The reason for this  $a$  overestimation tendency is most likely a slight bias in the  $t_{IA}$  measurements on one end or the other of the visible spectrum. Information presented in Table 3 suggests that the problem may lie in the short wavelength end of the spectrum (610-500 nm) and may involve sweep-level processing caveats. This  $a$  overestimation tendency is subject of ongoing research and further refinement of the sweep-level processing may correct this problem. Plots of the ratio of  $a$ 's between the various instruments (Figure 8) suggest that the discrepancy between the various instruments and the FRSR is particularly acute in clean air masses ( $t_{490-500A} < 0.2$ , although much of this apparent discrepancy is due to the uncertainty characteristics of  $a$  as discussed above. Nonetheless, it is doubtful that the degradation in the  $a$  comparisons is entirely due to the uncertainty considerations at low values of

$t_{490-500A}$ . This suggests that the FRSR tends to measure a steeper slope in  $t_{490-500A}$  ( $\mathbf{a}$ ) when the air mass is clean. The reasons for this bias are not clear, though unknown caveats in the sweep level processing may be partly responsible.

The analysis of  $t_{490-500A}$  is extended to all bands by computing the percentage of points for each instrument and channel that agree within uncertainty (Table 3). Initially, a matrix containing the percent agreement for each instrument combination in each overlapping band is computed. From this matrix, a sample-number weighted average of the percent agreement is calculated for each band. This serves the purpose of identifying suspect channels based on intra-instrument comparisons. The results show that there is excellent agreement in  $t_{IA}$  measurements collected with the hand-held sun photometers (>75%). Percent agreements are notably lower for comparisons of  $t_{410-412A}$  measured by Simbada and the FRSR. Otherwise, there is generally agreement between all instruments within uncertainties of at least 70% for  $t_{IA}$  and 90% for  $\mathbf{a}$ .

#### 4.0 Creating a Consensus Time Series of $t_{IA}$

To illustrate some of the basic caveats involved in arriving at a consensus value of  $t_{IA}$ , two time series' of the cloud-filtered data from the various instruments collected during two periods are analyzed (Figure 9). The ship was traversing clean maritime air during the first day (29 March 2001) and a polluted continental air mass during the second (9-10 April 2001). Inspection of the time series of  $t_{500A}$  (Figure 9a-b) suggests a larger variability in the FRSR data than the hand-held instruments in the clean air mass, but no systematic offset. In contrast, the FRSR measurements of  $t_{500A}$  are systematically lower in the polluted air mass than the handheld values. This offset is due to a deficiency in the FRSR technique in highly polluted air masses, as discussed previously. There is considerable variability in the measurements of  $\mathbf{a}$  in the clean air mass and excellent agreement in the polluted air mass. Considering the known uncertainties in measurements of  $\mathbf{a}$ , which are on the order of 0.6 in a clean maritime air mass (Miller et al., 2004), the measurements shown in the clean air mass, despite their spread, actually agree within uncertainties.

These two days are indicative of the nature of the multiple instrument time series through the range of conditions encountered aboard the R/V Ronald H. Brown during the ACE-Asia experiment and on many other cruises. There is enough internal consistency in the measurements to suggest that daily averages and statistics of  $t_{IA}$  and  $\mathbf{a}$  can be formed by combining the data from all five instruments with equal weighting. This procedure produces a time series of the daily geometric mean, geometric standard deviation, and extremes through the duration of the experiment. The geometric mean, rather than the arithmetic mean, is used because statistics of  $t_{IA}$  from long-term studies show a lognormal distribution (O'Neill et al., 2000; Ignatov and Stowe, 2001). This time series is hereafter referred to as the "consensus" time series of  $t_{IA}$  and  $\mathbf{a}$  (Figure 10).

A sampling issue is the relatively large number of data points generated by the FRSR relative to the hand-held sun photometers, whereupon the consensus time series could be biased by the FRSR. Results presented earlier suggest this bias has little impact

under most circumstances, but may have a minor impact in highly polluted conditions due to the difficulties encountered in the FRSR sweep processing.

The consensus time series quantifies a wide variety of conditions, including exceptional pollution in coastal areas. Aerosols are being sampled by a ship moving in a trajectory independent of wind flow, therefore encountering mesoscale features such as limiting streamlines in the wind field. Such streamlines can lead to sharp aerosol distribution gradients, which occurred in this case during the latter highly polluted portion of the cruise. Days with smaller values of  $t_{IA}$  show low variability, while polluted conditions have extremely high variability that cannot be adequately sampled using sparse data from the handhelds. Days 99 and 100 are examples of variable conditions encountered during these polluted conditions. The converse is true for  $a$ , since measurements are far more accurate in polluted conditions. Because the handhelds are not as exposed to the elements and typically have been calibrated more recently than the FRSR, they tend to provide a more accurate measurement of  $t_{IA}$  and  $a$ . Conversely, the FRSR is useful to evaluate aerosol homogeneity throughout the period to be averaged. A detailed statistical evaluation and scientific assay of R/V Ronald H. Brown ACE-Asia aerosol data will be presented in an upcoming companion paper.

To adequately describe the aerosol optical conditions at a given time during the ACE-Asia cruise aboard the Ronald H. Brown, or on any cruise, it is essential to understand the absolute values of  $t_{IA}$  and  $a$ , as well as the geometric variability for an appropriate window of time surrounding the observation. This criteria dictates that the most comprehensive characterization of the aerosol conditions will be made when complementary measurements are made with the FRSR and hand-held instruments. Failure to collect complementary data may result in unintended biases in the data set, depending on the application. For example, accurate aerosol optical measurements from a hand-held sun photometer may well represent the current conditions, but fail to capture the local variability in the air mass. Conversely, continuous measurements from an FRSR may provide an excellent survey of aerosol variability, but a less accurate measurement of  $t_{IA}$  and  $a$  due to a degraded calibration. The FRSR also provides important supporting measurements in the form of a dissection of the global irradiance into its direct-normal and diffuse components. Clearly, a complementary measurement effort with dutiful calibration and uncertainty consideration is the most accurate approach to marine sun photometry.

## 5.0 Conclusions

The results presented in this study validate the premise that all hand-held sun photometers employing the rigorous SIMBIOS measurement and calibration procedures (Fargion et al., 2001) produced statically identical measurements aboard the R/V Ronald H. Brown during ACE-Asia. Since many conditions were encountered during ACE-Asia, this conclusion is likely to be valid for most measurements at sea. Generally, the FRSR produced comparable results, although there is the potential for data processing related biases in high  $t_{IA}$  conditions. Results from this analysis have already inspired improvements in the FRSR data processing and further improvement is likely.

The largest difference between the FRSR and hand-held instruments is the sampling rate. The FRSR sampling period is two minutes, while hand-held sampling rates are determined by the operator and are typically much less frequent (several per hour under the best circumstances). The sampling rate is the fundamental issue in the selection of the appropriate device for a given application. The current SIMBIOS measurement protocol requires that a set of measurements (between nine and fifteen, depending on instrument) are made with properly configured instruments sequentially within an hour of satellite overpass (Knobelspiess et al. 2003). The ACE-Asia FRSR data suggest that this sampling strategy may not be adequate in rapidly changing, highly polluted conditions. Increasing the number and regularity of hand-held sun photometer measurement within an hour of satellite overpass increases the likelihood that aerosol conditions will be properly sampled. Operating the hand-held instruments with this protocol would be comparable in accuracy to the combination of high frequency FRSR and low frequency, but well calibrated, hand-held sun photometer measurements. Such a sampling strategy is only feasible due to operator limitations for short periods such as a one-hour window required for satellite comparison.

Frequency distributions of  $t_{IA}$  and  $\mathbf{a}$  for the entire experiment period reveal some systematic biases. The frequency distributions of  $t_{490-500A}$  and  $t_{870A}$  for the experiment are remarkably similar despite the different sampling strategies of the FRSR and hand-helds (Figure 11). The most notable feature of the histograms is the relatively larger frequency of measurements with  $t_{IA} < 0.2$ . Although large uncertainty is assigned to measurements when  $t_{IA} < 0.2$ , which complicates the interpretation of this region of air mass phase space, uncertainty arguments are not sufficient to explain the observed biases. The prevalence of marine boundary layer clouds in clean, maritime air masses may be an important contributor to the observed bias. When clouds are present, the operator of the hand-held may be able to judiciously collect observations during clear periods, while the FRFR automated cloud filtering algorithm may reject the observations if the filtering criteria are not met. Despite the systematic underestimate of  $t_{IA}$  by the FRSR demonstrated earlier, the frequency distributions of  $t_{IA}$  suggest that these highly polluted conditions are observed so infrequently that the impact on the experiment statistics is minimal.

In contrast to the excellent agreement in the histograms of  $t_{IA}$ , histograms of  $\mathbf{a}$  reveal significant biases (Figure 11c). Specifically, the frequency distributions from the FRSR and the hand-held sun photometers have peaks at different values of  $\mathbf{a}$ . This offset cannot be attributed to the observed differences in the frequency distributions of  $t_{IA}$  when  $t_{IA} < 0.2$ , as described above, because  $\mathbf{a}$  is typically small ( $\mathbf{a} < 0.5$ ) in clean maritime air masses. Moreover, the large uncertainty associated with computing  $\mathbf{a}$  in a clean, maritime air mass makes it impossible to distinguish between the two peaks in the frequency distribution. The  $\mathbf{a}$  measurements agree within uncertainty when  $\mathbf{a} < 0.5$ . The impact of the observed differences in the frequency distributions of  $t_{IA}$  when  $t_{IA} < 0.2$  is confined the phase space in the  $\mathbf{a}$  histogram where  $\mathbf{a} < 0.5$ . Therefore, the clean maritime air mass bias cannot explain the observed offset in the peaks of the frequency distributions of  $\mathbf{a}$  when  $\mathbf{a} > 0.5$ . In this circumstance, the histograms show

that the FRSR has a peak in its  $a$  frequency distribution at values that are 0.3 larger than the peak for the hand-held units. In addition, there is a tail in the FRSR frequency distribution when  $a > 1.5$  that does not exist in the frequency distributions of the hand-held units. Notably, both frequency distributions exhibit a similar bi-modal shape, though the distribution for the hand-held units is considerably narrower.

One reason for the differences in the frequency distributions of  $a$  is the underlying method that is used to compute  $a$  (Figure 11c-d). When  $a$  is computed using the two-band method (Figure 11d), the frequency distributions of  $a$  for the FRSR and the hand-held sun photometers show considerably better agreement and the width of the two frequency distributions is similar, though the peaks in the two distributions remain offset. There is some overlap in the distributions surrounding the peaks, which is not present when the line fitting method is used (i.e. the peaks are more narrow; Figure 11c). The differences observed when the line-fit method is used may be generated by any or all of the following conditions: (1) differences in the spectral resolution of the information in the 560-680 nm range supplied by the hand-held sun photometers and by the FRSR, (2) one or more poorly calibrated channels in the 560-680 nm range, or (3) technique-related biases that are observed only in the 560-680 nm range. This analysis shows that the statistical distribution of  $a$  during this experiment is different for the combined data from the hand-held sun photometers and the FRSR, and that these differences may arise from a combination of factors.

The data collected aboard the R/V Ronald H. Brown during ACE-Asia provided a rigid test of different marine sun photometers and techniques. A wide range of aerosol conditions was encountered, including clean maritime conditions and highly polluted coastal environments. The results of this study suggest that the use of either hand-held or FRSR marine sun photometers to measure  $t_{IA}$  will yield similar results if proper measurement protocols are used and if the instruments are properly calibrated.

## 6.0 References

- Ackerman, S.A., O.B. Toon, D.E. Stevens, A.J. Heymsfield, V. Ramanathan, and E.J. Welton, 2000: Reduction of tropical cloudiness by soot. *Science*, **288**, 1042-1047.
- Albrecht, B.A., 1989: Aerosols, cloud microphysics, and fractional cloudiness. *Science*, **245**, 1227-1230.
- Ångström, A.K., 1929: On the atmospheric transmission of sun radiation and on dust in the air, *Geogr. Ann. H.2*.
- Ångström, A., 1961: Techniques for determining the turbidity of the atmosphere, *Tellus*, **2**, 214-223.
- Chameides, W.L., H. Yu, S.C. Liu, M. Bergin, X. Zhou, L. Mearns, G. Wang, C.S. Kiang, R.D. Saylor, C. Luo, Y. Huang, A. Steiner, and F. Giorgi, 1999: Case study of the effects of atmospheric aerosols and regional haze on agriculture: an opportunity to enhance crop yields in China through emission controls. *PNAS*, **96**, 13626-13633.
- Deschamps P.-Y., P. Lecomte, C. Verwaerde, B. Fougnie, and R. Frouin, 2002: SIMBAD: a field radiometer for satellite ocean-color validation. *Applied Optics*, (submitted).

- Draxler, R.R. Hybrid single-particle Lagrangian integrated trajectories (HY-SPLIT): Version 3.0, Users Guide and Model Description, Tech. Rep. ERL ARL-195, National Oceanic and Atmospheric Administration, Silver Springs, Md., 1992.
- Fargion, G., R. Barnes, and C. McClain, In Situ Aerosol Optical Thickness Collected by the SIMBIOS Program (1997-2000): Protocols, and Data QC and Analysis. *NASA Tech. Memo. 2001-209982*, NASA Goddard Space Flight Center, Greenbelt, Maryland, 11-21.
- Gordon, H.R. and M. Wang, 1994: Retrieval of water-leaving radiance and aerosol optical thickness over the oceans with SeaWiFS: a preliminary algorithm, *Applied Optics*, **33**, 443-452.
- Hansen, J.E., M.Sato, and R.Reudy, 1997: Radiative forcing and climate response. *J. Geophys. Res.*, **102**, 6831-6864.
- Ignatov, A. and L. Stowe, 2001: Aerosol Retrievals from Individual AVHRR Channels. Part II: Quality Control, Probability Distribution Functions, Information Content, and Consistency Checks of Retrievals, *J. Atmos. Science*, **59**, 335-362.
- Junge, C., 1955: The size distribution and aging of natural aerosol as determined from electrical and optical data on the atmosphere, *J. Meteorol.*, **12**, 13-25.
- Knobelspiesse, K.D., C. Pietras, G.S. Fargion, M. Wang, R. Frouin, M.A. Miller, A. Subramaniam and W.M. Balch, 2003: Maritime aerosol optical properties measured by handheld sun photometers. *Remote Sen. of Env.* (submitted).
- Long, C.N., D.L. Slater, and T. Tooman, 2001: Total sky imager model 880 status and testing results; US Department of Energy Atmospheric Radiation Measurement Program Technical Report, TR-006, pp. 36.
- Markowitz, K.M., P.J Flatau, P.K. Quinn, C.M. Carrico, M.K. Flatau, A.M. Vogelmann, D. Bates, M. Liu, and M. Rood, 2003: Influence of relative humidity on aerosol radiative forcing: an ACE-Asia experiment perspective, *J. Geophys. Res.*, **108**, 8662.
- Miller, M.A., M.J. Bartholomew, and R.M. Reynolds, 2004: The accuracy of marine shadow-band measurements of aerosol optical thickness and Ångström exponent. *J. Atmos. Ocean. Tech.* (in press).
- Morys, M., F. M. Mims III, S. Hagerup, S. E. Anderson, A. Baker, J. Kia, and T. Walkup, 2001: Design, calibration, and performance of MICROTOPS II handheld ozone monitor and sun photometer, *J. Geophys. Res.*, **106**, 14,573-14,582.
- NRC, National Research Council, *Aerosol Radiative Forcing and Climatic Change*, National Academy Press, Washington, D.C., 1996.
- O'Neill, N.T., A. Ignatov, B. Holben and T. Eck, 2000: The log-normal distribution as a reference for reporting aerosol optical depth statistics; empirical tests using multi-year, multi-site AERONET sun photometer data. *Geophys. Res. Lett.*, **27**, 3333-3336.
- Pietras et al., 2002
- Porter, J.N., M.A. Miller, C. Motell, and C.Pietras, 2001: Use of hand-held sun photometers for measurements of aerosol optical thickness at sea. *J. Atmos. Ocean. Tech.* Vol. 18, 765-774.
- Reynolds, M.R., M.A. Miller, and M.J. Bartholomew, 2001: A fast-rotating, spectral shadowband radiometer for marine applications. *J. Atmos. Ocean. Tech.*, Vol. 18, No. 2, 200-214

- Shettle, E.P. and R.W. Fenn, 1979: Models for the aerosols of the lower atmosphere and the effects of humidity variations on their optical properties, Air Force Geophysics Laboratory, AFGL-TR-79-0214, 676, pp.94.
- Sokolik, I.N., and O.B. Toon, 1999: Incorporation of mineralogical composition into models of the radiative properties of mineral aerosol from UV to IR wavelengths. *J. Geophys. Res.*, 104, 9423-9444.
- Stephens, G.L., 1994: *Remote Sensing of the Lower Atmosphere*, Oxford University Press, pp. 523.
- Thuillier, G., M. Herse, P.C. Simon, D. Labs, H. Mandel, D. Gillotay, and T. Foujols, 2002: The solar spectral irradiance from 200 to 2400 nm as measured by the SOLSPEC spectrometer from the ATLAS 1-2-3 and EURECA missions. *Solar Physics*
- Twomey, S., 1977. The influence of pollution on the shortwave albedo of clouds. *J. Atmos. Sci.*, 34, 1149-1152.
- Voss, K.J., E.J. Welton, P.K. Quinn, R. Frouin, M.A. Miller, and R.M. Reynolds, 2001: Aerosol optical depth measurements during the Aerosols99 experiment, *J. Geophys. Research*, 106, 20811-20820.

## 6.0 Tables

Table 1. Sun photometers deployed on R/V Ronald H. Brown during ACE-Asia.

Instrument	Center wavelengths, per band (nm)											
Simbad #03				443	490		560		670		870	
SimbadA #02	350	380	412	443	490	510	560	620	670	750	870	
Microtops #3773				440	500				675		870	936
Microtops #4080		380		440	500				675		870	
Fast Rotating Shadowband Radiometer			410		500			615	680		870	940

\*SIMBIOS Project sun photometers are calibrated on land by a cross calibration to CIMEL sun photometers maintained by the AERONET Project. The CIMEL sun photometers are calibrated with the Langley method at Mauna Loa

\*\*The calibration of this instrument is tied to satellite-measure extra-terrestrial irradiance (Miller et al, 2003)

Table 2. Calibration information for hand-held radiometers used in this study

Sun photometer SN	Date	Calibration Technique	Site	PI Name
Microtops #3773	Sep 20 2000	Cross Calibration	NASA/GSFC	J. Welton/K. Knobelspiesse
	July 06 2001	Cross Calibration	NASA/GSFC	
Microtops #4080	Prior cruise	Langley-Bouguer	Mauna Loa	P. Quinn/Trish Quinn
	5 months later	Langley-Bouguer	Mauna Loa	
Simbad #03	Dec 30 2000	Langley-Bouguer	Mt Stevenson	R. Frouin
	Jun 28 2001	Langley-Bouguer	Mt Stevenson	
Simbada #02	March 8 2001	Langley-Bouguer	Mt Stevenson	P. Y. Deschamps
	May 01 2001	Langley-Bouguer	Mt Stevenson	

Table 3: Percentage of ACE-Asia concurrent measurements that fall within calculated uncertainties

Instrument and Wavelength in nm or Measurement	Weighted Averages
SIMBAD 443	88.8
“” 490	83.9
“” 560	90.1
“” 670	79.9
“” 870	85.0
“” Ångström	97.3
SIMBADA 412	98.8
“” 443	87.8
“” 490	84.6
“” 560	90.1
“” 620	73.6
“” 670	75.0
“” 870	80.3
“” Ångström	92.1
SIMBIOS Microtops II 440	85.4
“” 500	82.5
“” 675	86.7
“” 870	89.8
“” Ångström	97.6
NOAA-PMEL Microtops II 440	74.7
“” 500	70.9
“” 675	69.0
“” 870	57.3
“” Ångström	84.5
FRSR 410	98.8
“” 500	73.1
“” 615	73.6
“” 680	78.4
“” 870	89.6
“” Ångström	98.2

## LIST OF FIGURES

Figure 1. Cruise trajectory of the RV Ronald H. Brown during ACE-Asia. Latitudes and longitudes are indicated and the cruise trajectory is color coded according to the type of aerosol suggested by a trajectory analysis. The types of aerosol present are given in the accompanying legend. (a) the complete cruise trajectory, and (b) a close-up of the cruise trajectory in the vicinity of Japan.

Figure 2. Comparison plots of  $t_{IA}$  at the specified wavelength for the hand-held marine sun photometers. Each data point represents a direct comparison between the two instruments during 15-minute windows. The total number of comparison points is indicated beneath the graph along with the percentage that agreed within uncertainty. (a) the Simbad vs. SimbadA 490 nm channels, (b) the SimbadA 490 nm vs. the SIMBIOS Microtops 500 nm channel, and (c) the SIMBIOS Microtops 500 nm channel vs. the Simbad 490 nm channel.

Figure 3. As in Figure 2, but for  $a$ .

Figure 4. Comparison plots of the ratio of  $a$  for the instruments listed on the y-axis against the average  $t_{IA}$  (490 and 500 nm center wavelengths averaged together). Each data point represents a direct comparison between the two instruments during 15-minute windows. The total number of comparison points is indicated beneath the graph along with the percentage that agreed within uncertainty. (a) the Simbad-SimbadA  $a$  ratio, (b) the SimbadA-SIMBIOS Microtops  $a$  ratio, and (c) the SIMBIOS Microtops/ Simbad  $a$  ratio.

Figure 5. Comparison plots of  $t_{IA}$  at the specified wavelength for the FRSR and hand-held marine sun photometers. Each data point represents a direct comparison between the two instruments during 15-minute windows. The total number of comparison points is indicated beneath the graph along with the percentage that agreed within uncertainty. (a) the Simbad 490 nm vs. FRSR 500 nm channel, (b) the SIMBIOS Microtops 500 nm channel vs. FRSR 500 nm channel, and (c) the Simbad 490 nm channel vs. FRSR 500 nm channel.

Figure 6. (a) A plot of the time series of voltage counts from the FRSR for each sweep that passed quality control during a two-minute sampling window. These individual sweeps are used to determine the direct-normal irradiance. The red circles represent the voltages selected by the FRSR processing as representative of the “edge” voltage (Reynolds et al, 2001; Miller et al, 2003). A visible sky images from the TSI for one of the individual sweeps from (a) the Northern Pacific Ocean in a clean air mass ( $t_{IA}$  =0.08 at 500 nm) and (b) the polluted air mass above the Sea of Japan ( $t_{IA}$  =0.98 at 500 nm).

Figure 7. Comparison plots of  $a$  at the specified wavelength for the hand-held marine sun photometers. Each data point represents a direct comparison between the two instruments during 15-minute windows. The total number of comparison points is

indicated beneath the graph along with the percentage that agreed within uncertainty. (a) the Simbad vs. SimbadA 490 nm channels, (b) the SimbadA 490 nm vs. the SIMBIOS Microtops 500 nm channel, and (c) the SIMBIOS Microtops 500 nm channel vs. the Simbad 490 nm channel.

Figure 8. Comparison plots of the ratio of  $\mathbf{a}$  for the instruments listed on the y-axis against the average  $t_{IA}$  (490 and 500 nm center wavelengths averaged together). Each data point represents a direct comparison between the two instruments during 15-minute windows. The total number of comparison points is indicated beneath the graph along with the percentage that agreed within uncertainty. (a) the Simbad-SimbadA  $\mathbf{a}$  ratio, (b) the SimbadA-SIMBIOS Microtops  $\mathbf{a}$  ratio, and (c) the SIMBIOS Microtops/ Simbad  $\mathbf{a}$  ratio.

Figure 9. (a) Time series of  $t_{IA}$  for 29 March 2001 from the FRSR (blue squares), Microtops with custom algorithm (red diamonds), Simbad (green pluses), SimbadA (blue asterisk), and Microtops without the custom algorithm (black triangles). The blue circle with the vertical line represents typical uncertainties for these measurements; (b) as in (a) but for 9-10 April 2001; (c) as in (a) but for  $\mathbf{a}$ ; (d) as in (b), but for  $\mathbf{a}$ .

Figure 10. (a) Plot of  $t_{IA}$  at 870 nm classified by trajectory-based air mass type. The different air masses are plotted according to the color codes in Figure 1 and with different symbols; (b) Time series of the geometric statistics of cloud-filtered  $t_{IA}$  at 500 nm for a one-hour window around local noon. The whisker plots show the geometric mean (center bar), the geometric standard deviations (upper and lower bounds of box), and the lines above and below represent the maximum and minimum observed values; (c) as in (b) but for 670 nm; (d) as in (b), but for 870 nm; (e)  $\mathbf{a}$  for the experiment period.

Figure 11. Histograms of  $t_{IA}$  and  $\mathbf{a}$  for the R/V Ronald H. Brown cruise during ACE-Asia. The dotted line represents the histogram of the hand-held data and the solid line the FRSR data. The bin width for  $t_{IA}$  is 0.05 and the bin width for  $\mathbf{a}$  is 0.1. (a)  $t_{490-500A}$  (490 and 500 nm center wavelengths averaged together), (b)  $t_{870A}$ , (c)  $\mathbf{a}$  computed by fitting a line through all measurements of  $t_{IA}$ , and (d)  $\mathbf{a}$  computed by using only two bands ( $t_{490-500A}$  and  $t_{870A}$ ).

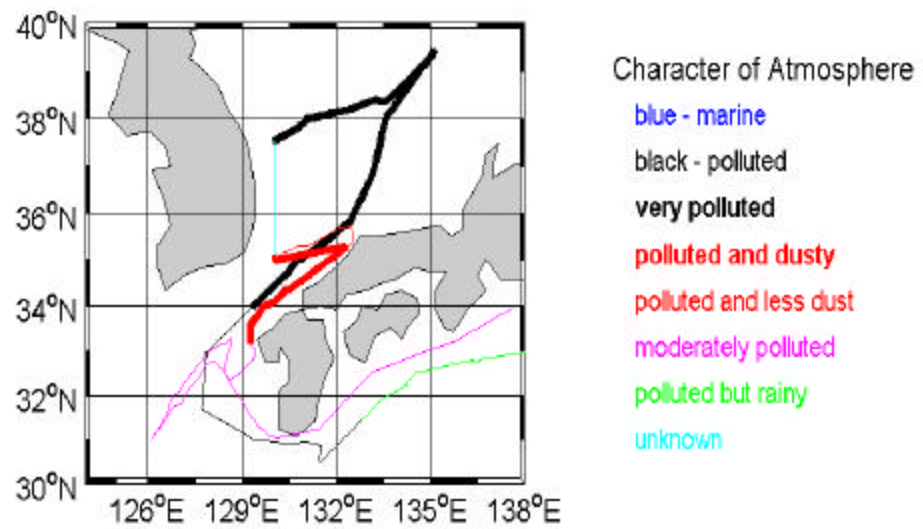
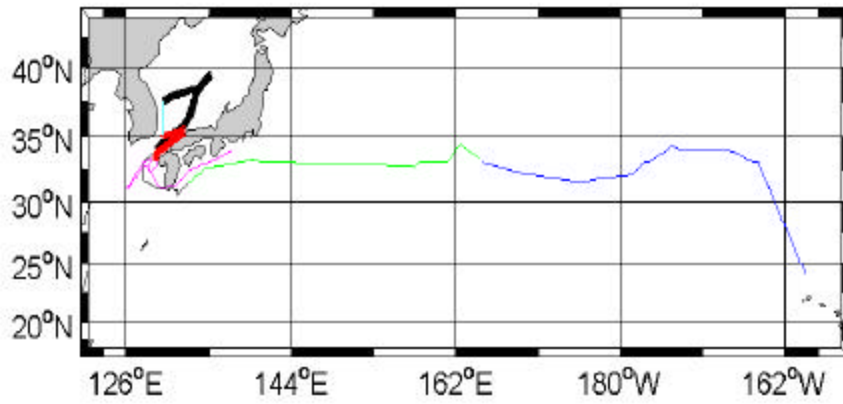
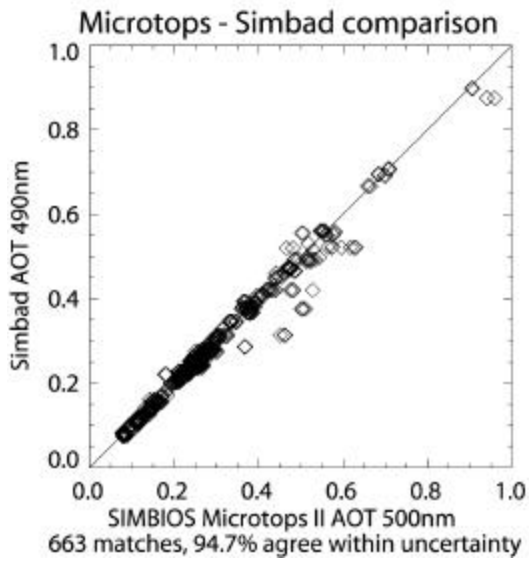
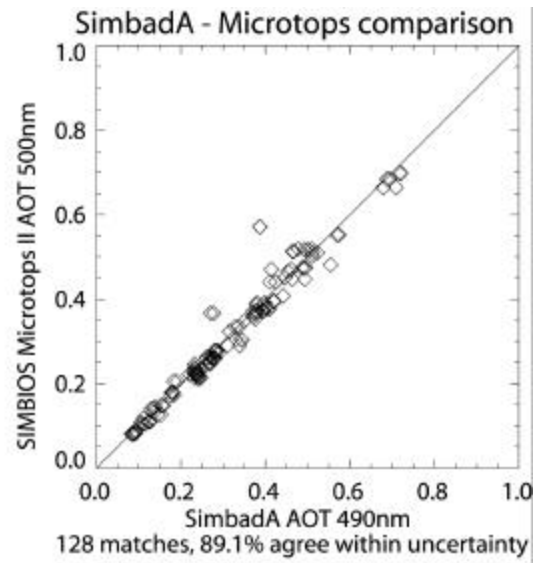
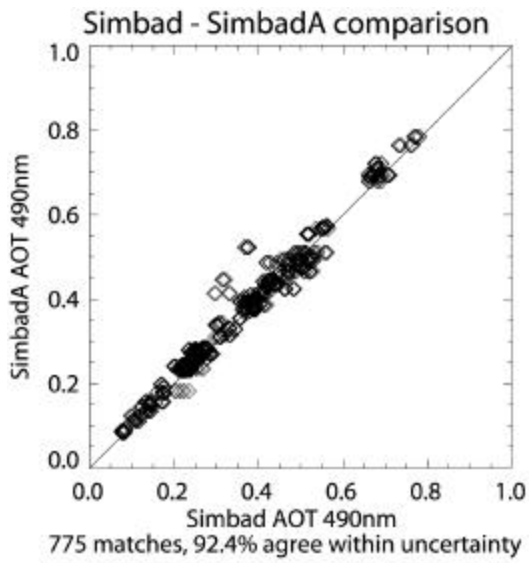
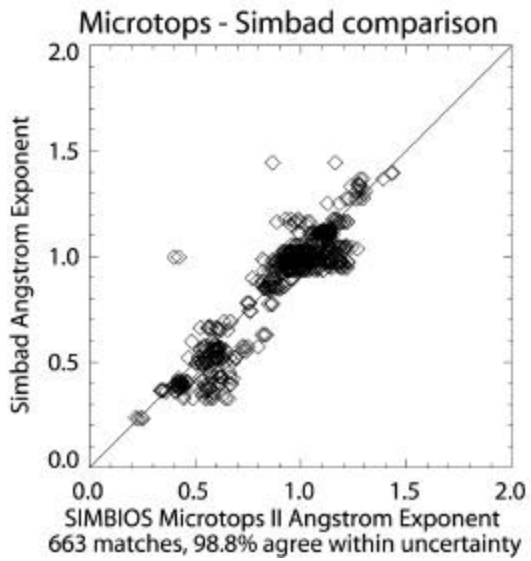
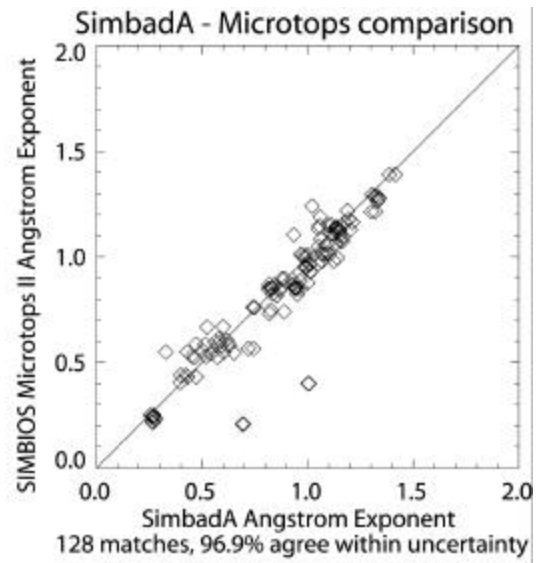
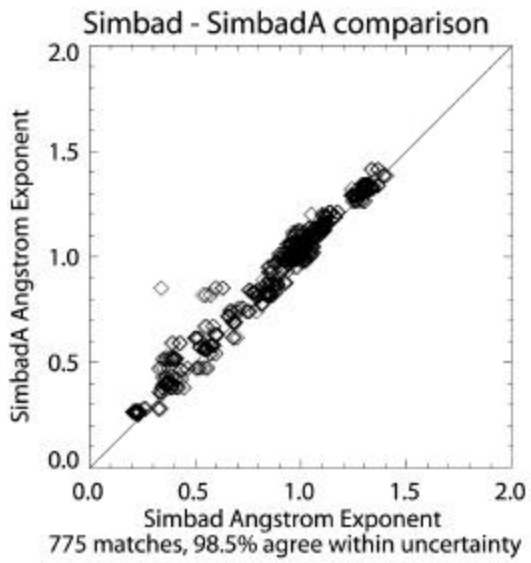


FIGURE 1



**FIGURE 2**



**FIGURE 3**

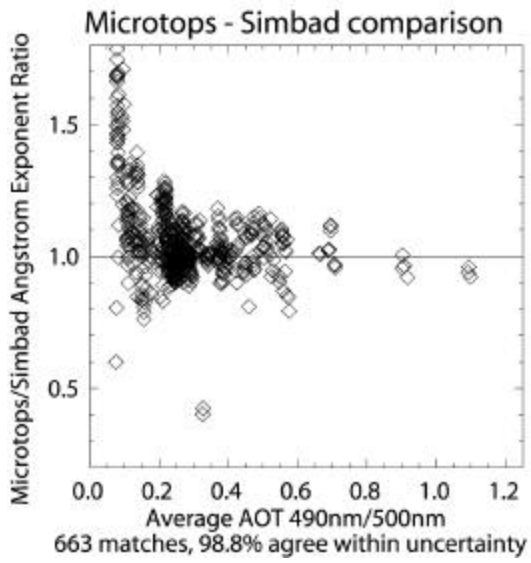
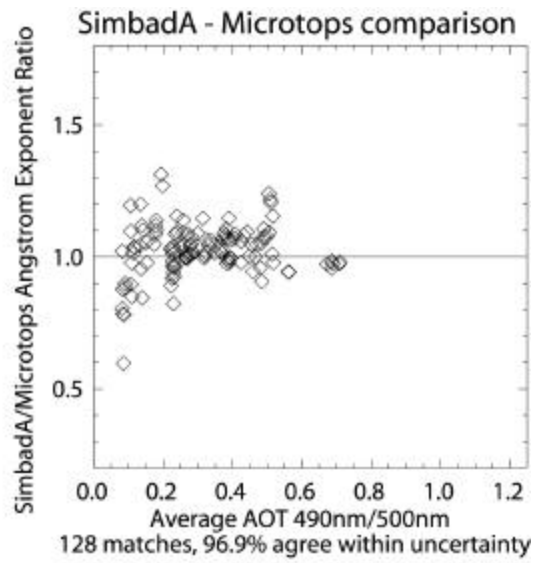
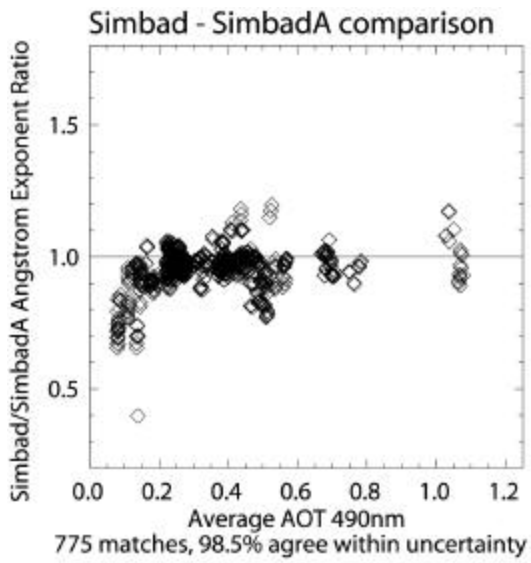


**FIGURE 4**

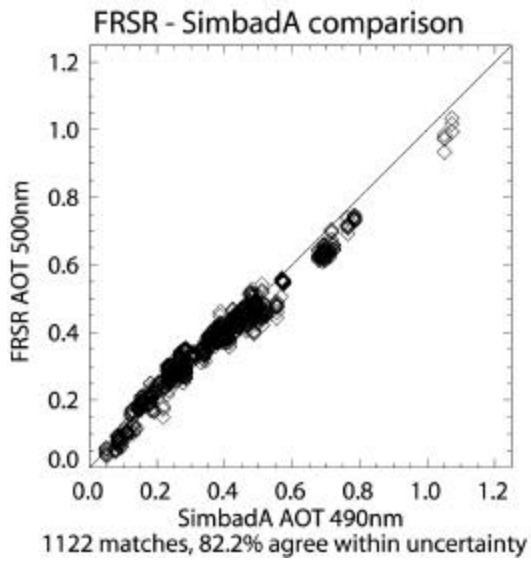
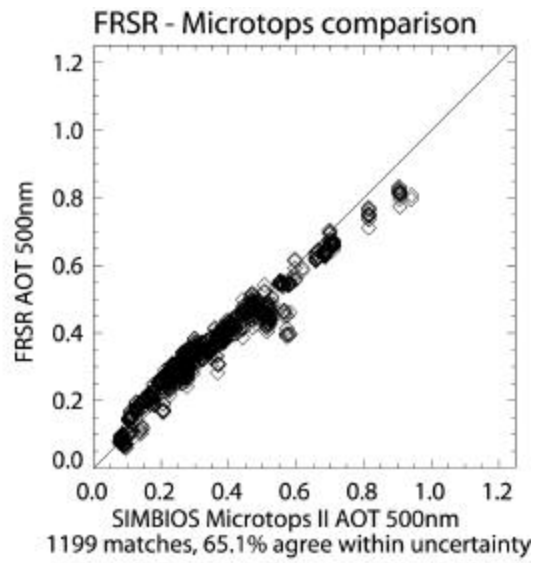
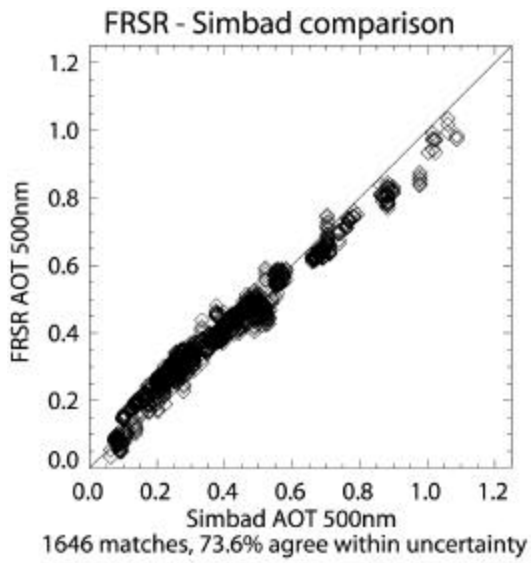
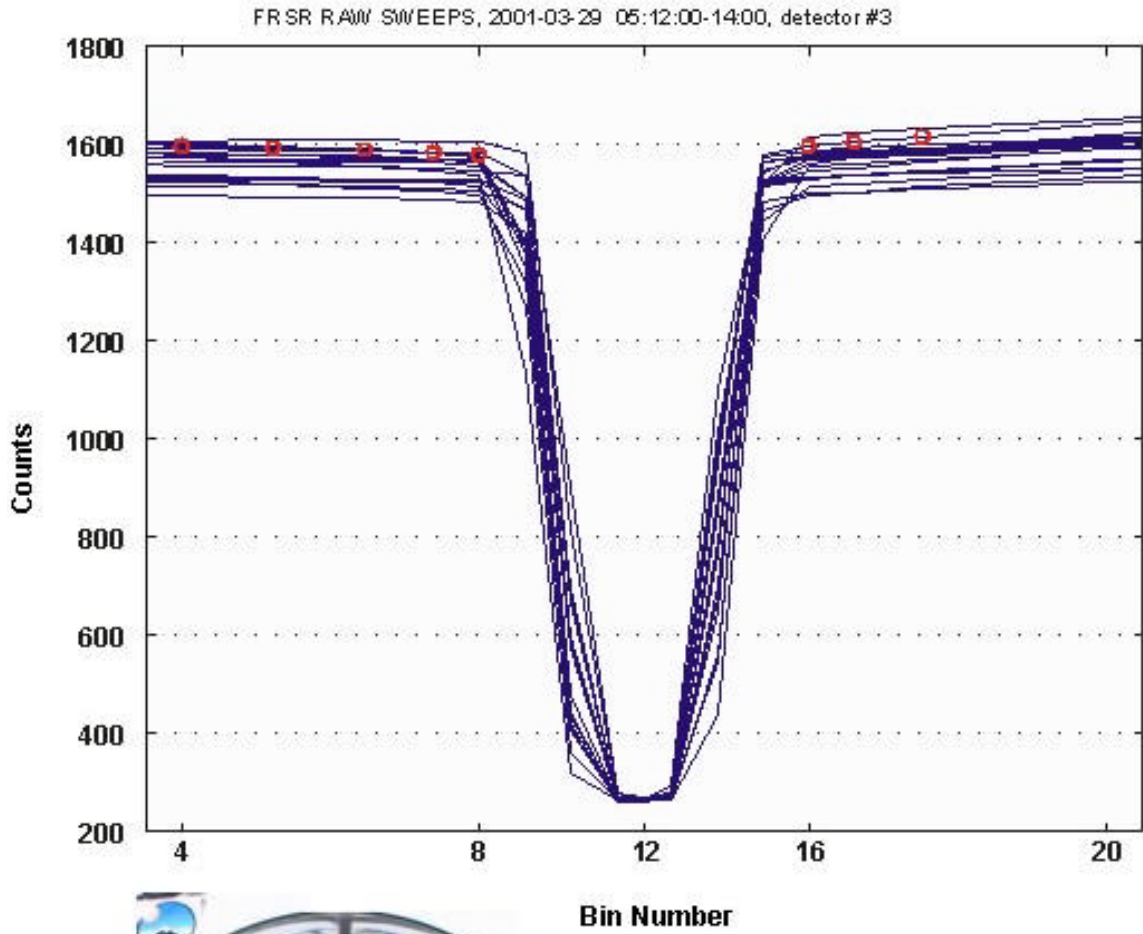


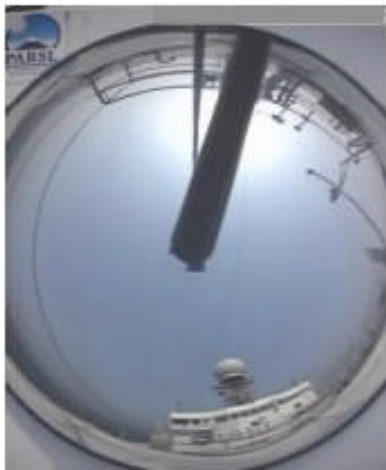
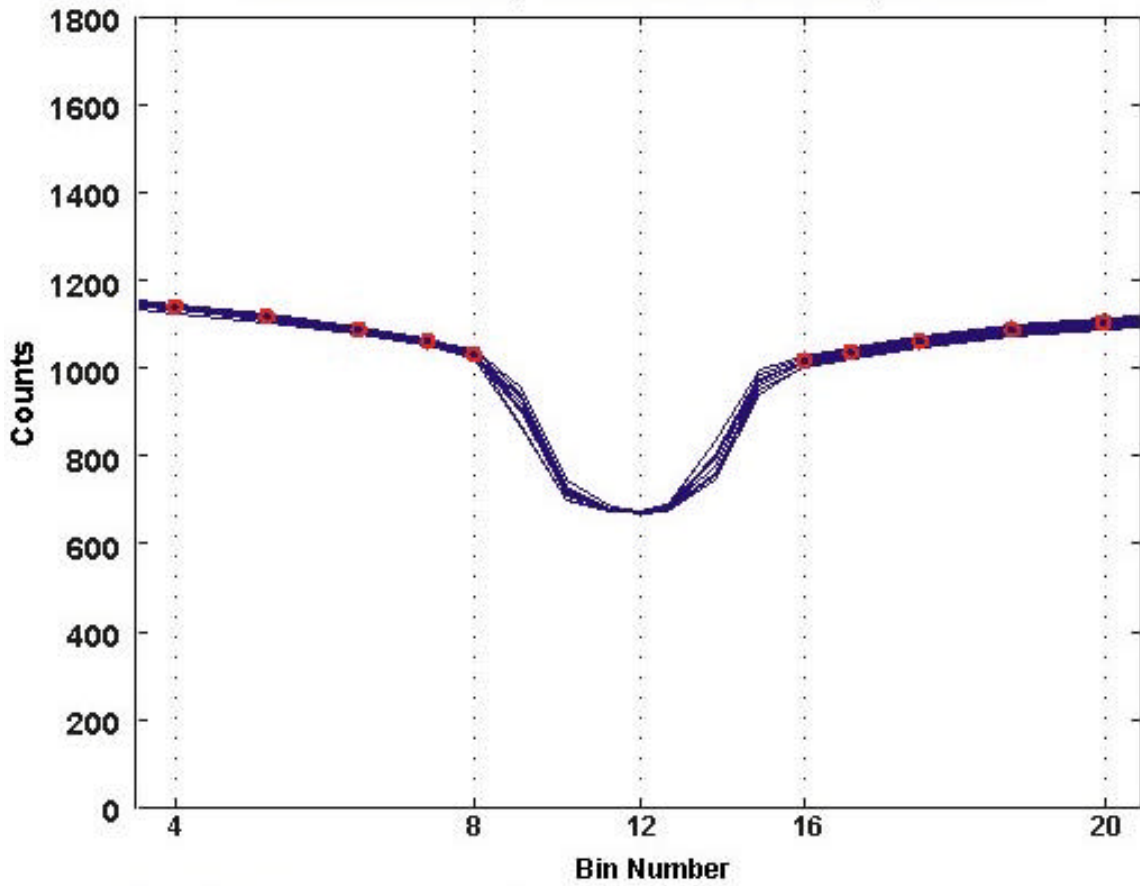
**FIGURE 5**



$\lambda_{\text{ot}} 500\text{nm} = 0.08$   
 $d/n = 0.14$   
 zenith = 51.0 degrees

FIGURE 6a

FRSR RAW SWEEPS, 2001-04-09 06:06:00-08:00, detector #3



$\text{aot } 500\text{nm} = 0.98$   
 $d/n = 1.74$   
zenith = 50.8 degrees

FIGURE 6b

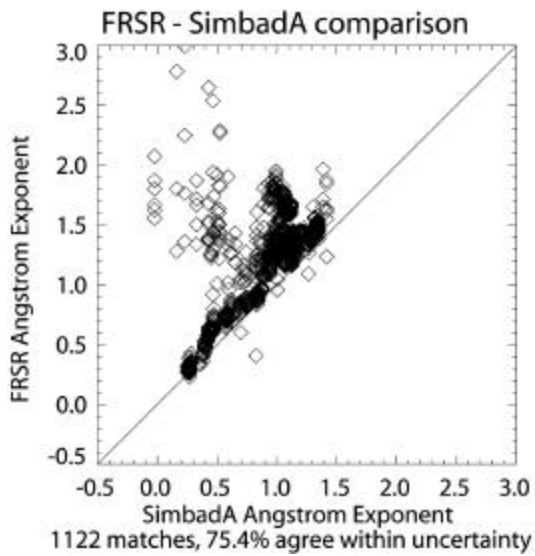
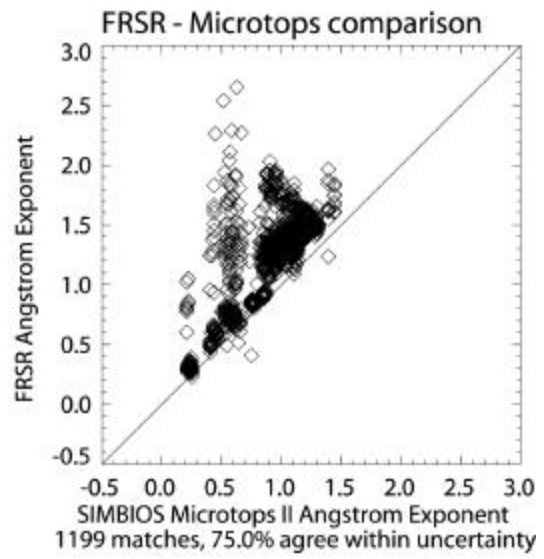
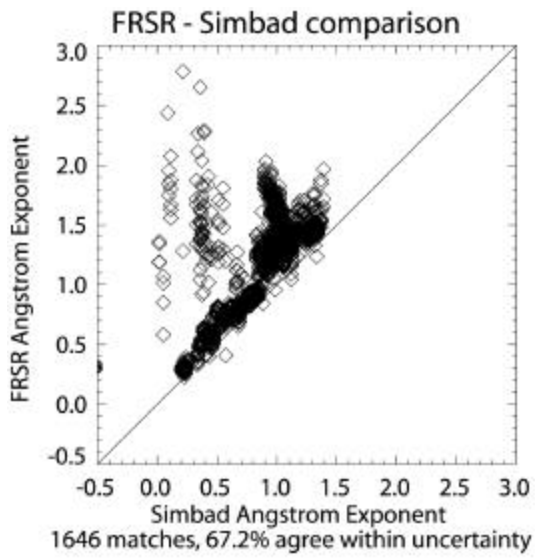


**FIGURE 7**

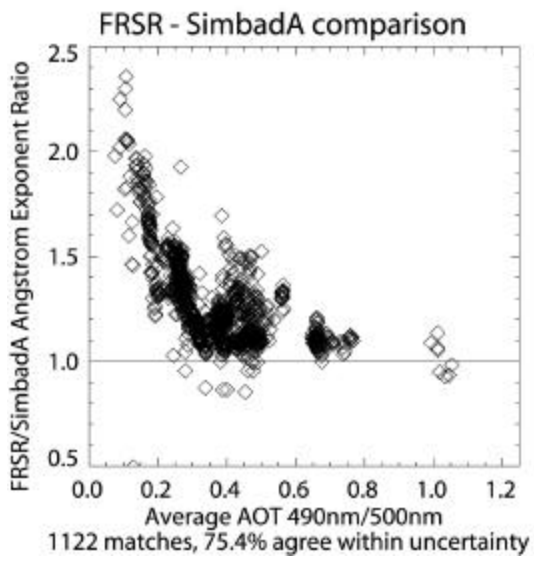
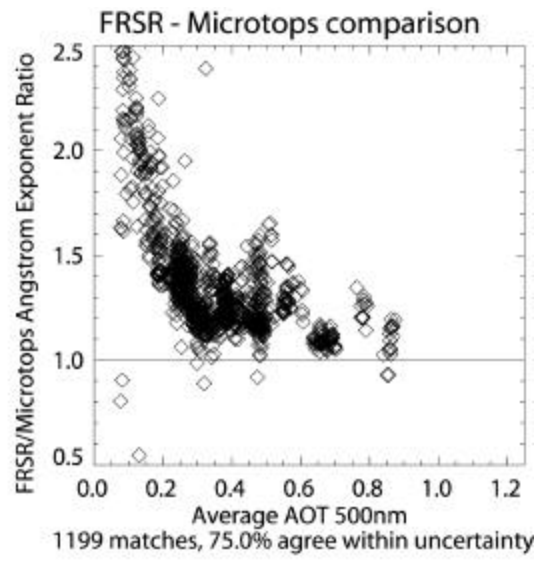
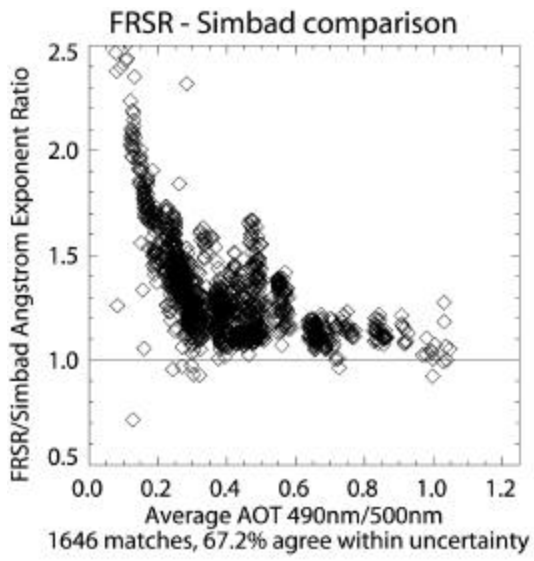


**FIGURE 8**

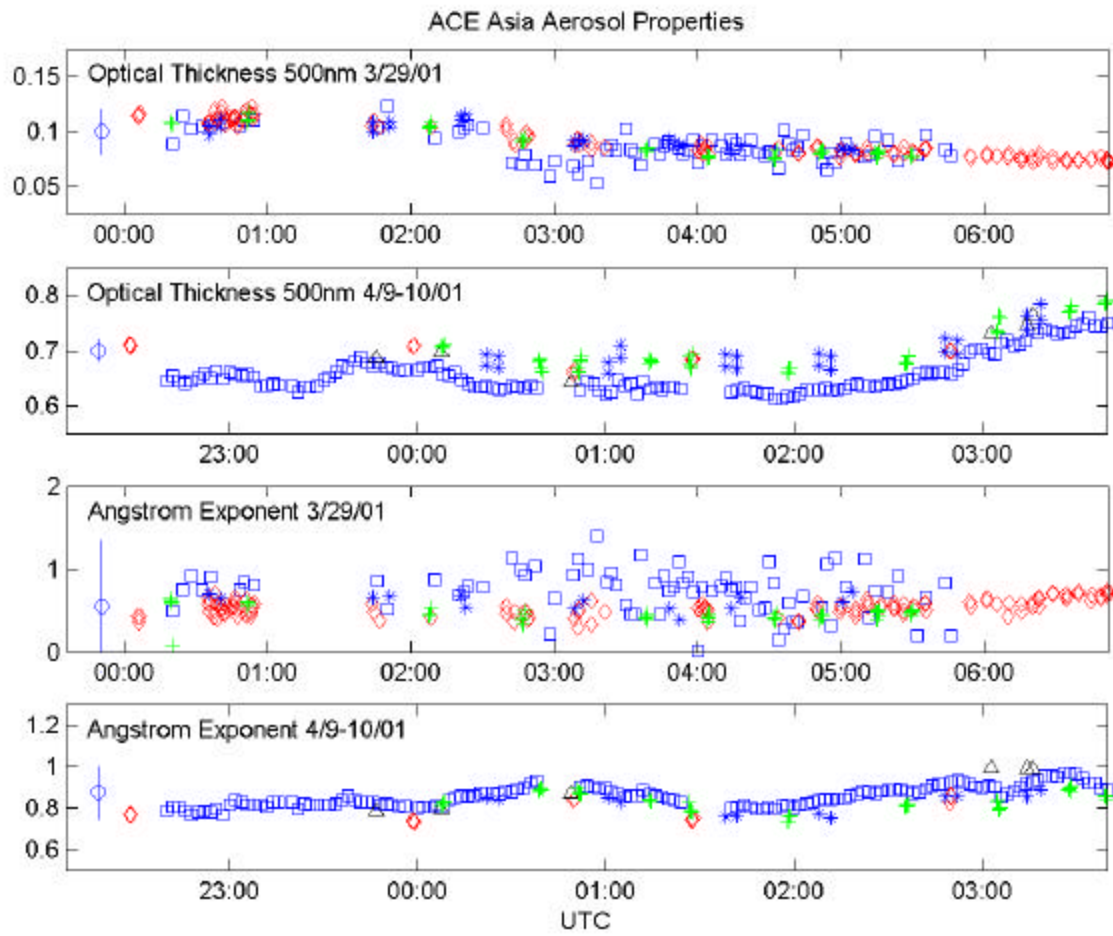


**FIGURE 9**

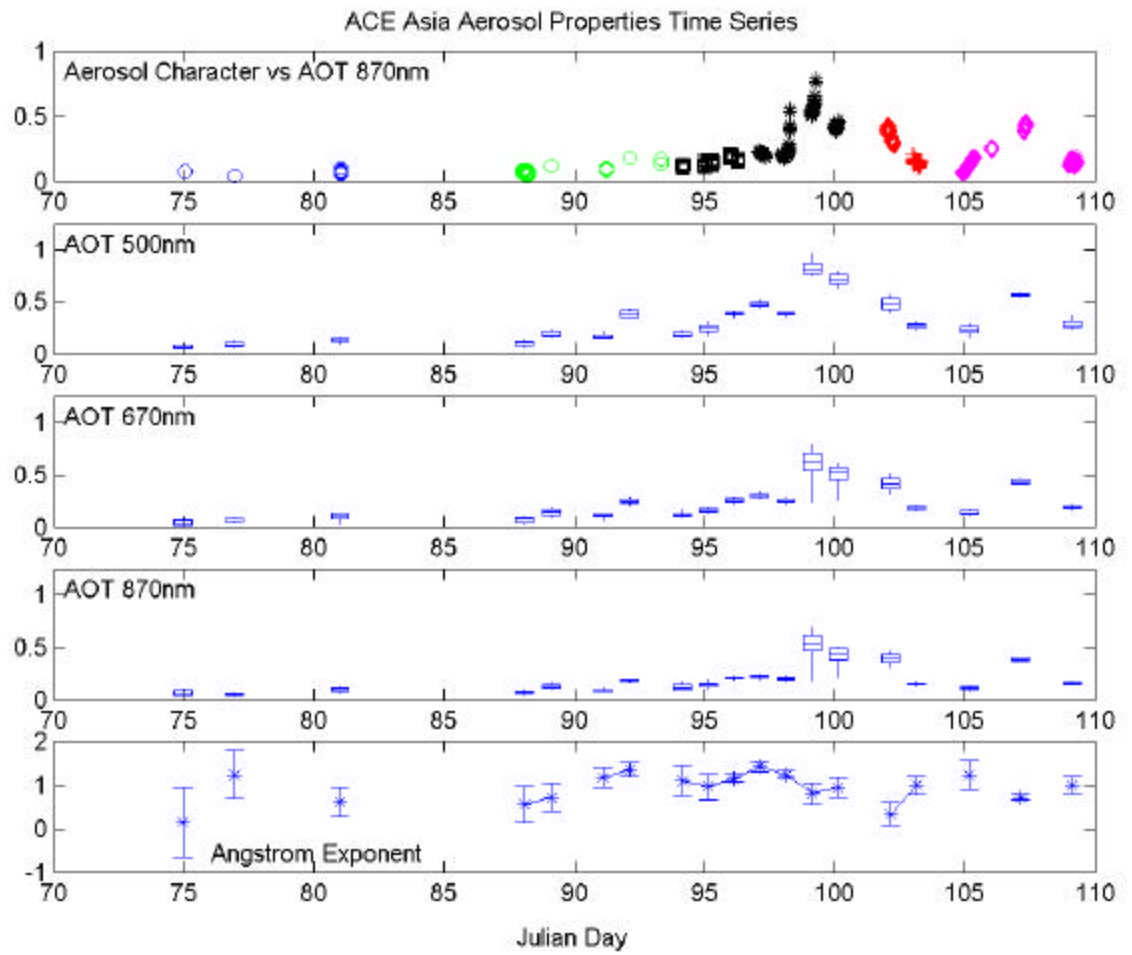


**FIGURE 10**

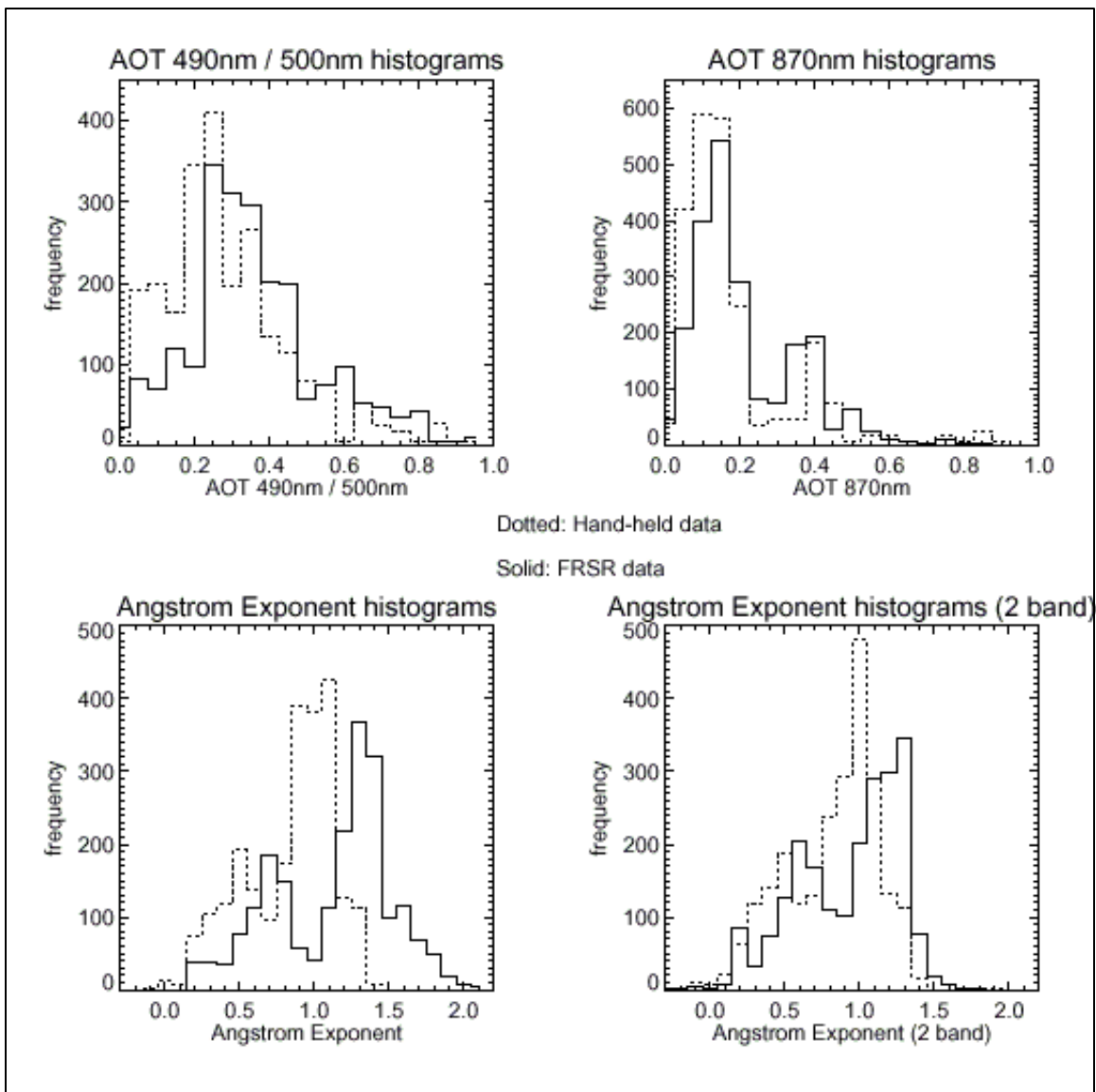


FIGURE 11